Research Article
Vol. 14, No. 2 / 1 Feb 2023 / *Biomedical Optics Express* 883
Biomedical Optics EXPRESS

Localized transverse flow measurement with dynamic light scattering line-scan OCT

LE HAN,[1] BINGYAO TAN,[2,3,4] LEOPOLD SCHMETTERER,[2,3,4,5,6,7,8] AND KOSTADINKA BIZHEVA[1,9,10,*]

[1] *Department of Physics and Astronomy, University of Waterloo, Waterloo, Ontario N2L 3G1, Canada*
[2] *School of Chemistry, Chemical Engineering and Biotechnology, Nanyang Technological University, 639798, Singapore*
[3] *SERI-NTU Advanced Ocular Engineering (STANCE), 639798, Singapore*
[4] *Singapore Eye Research Institute, Singapore National Eye Center, 169856, Singapore*
[5] *Ophthalmology & Visual Sciences Academic Clinical Program, Duke-NUS Medical School, Singapore*
[6] *Institute of Molecular and Clinical Ophthalmology, Basel, Switzerland*
[7] *Department of Clinical Pharmacology, Medical University Vienna, Vienna, Austria*
[8] *Center for Medical Physics and Biomedical Engineering, Medical University Vienna, Vienna, Austria*
[9] *Dept. of Systems Design Engineering, University of Waterloo, Waterloo, Ontario N2L 3G1, Canada*
[10] *School of Optometry and Vision Sciences, Univ. of Waterloo, Waterloo, Ontario N2L 3G1, Canada*
[*] *kbizheva@uwaterloo.ca*

Abstract: A novel decorrelation-based approach for measuring localized transverse flow velocity using line-scan (LS) optical coherence tomography (OCT) is proposed. The new approach allows for separation of the flow velocity component along the line-illumination direction of the imaging beam from other orthogonal velocity components, from particle diffusion motion, and from noise-induced distortion in the OCT signal's temporal autocorrelation. The new method was verified by imaging flow in a glass capillary and a microfluidic device and mapping the spatial distribution of the flow velocity within the beam's illumination plane. This method can be extended in the future to map the three-dimensional flow velocity fields for both ex-*vivo* and *in-vivo* applications.

1. Introduction

OCT can map blood perfusion and measure blood flow velocity in biological tissues, which is believed to be an important biomarker for many diseases [1]. Based on whether it generates qualitative or quantitative results, the OCT-based blood flow imaging can be classified into OCT angiography (OCTA) [2–5] and OCT-based velocimetry [6–11] respectively. OCTA utilizes the intensity or phase variance to separate blood vessels from static tissues. However, the OCTA signal provides limited information about the flow dynamics as acquisition of multiple B-scans from the same location over time utilized in the OCTA methods leads to complete decorrelation of the signal at the location where flow is measured. The OCT methods for measuring localized flow velocity can be divided into two categories: phase-based Doppler OCT [6–8] and dynamic light scattering (DLS) OCT techniques [9,10].

Since OCT is a heterodyne detection technique, the complex OCT signal contains phase information regarding the depth location of the imaged scatters. Measuring spatially resolved flow velocity is possible by tracking the temporal phase distribution of the detected scattered light. However, conventional Doppler OCT (DOCT) is only sensitive to phase changes in the axial direction; therefore, total flow velocity cannot be measured precisely for many applications of Doppler OCT due to ambiguity in determining the Doppler angle – the angle between the imaging beam and the flow velocity [12]. In addition, when the Doppler angle is close to 90 degrees, the axial motion induced phase change could be smaller than the phase noise of the

#484257
Journal © 2023
https://doi.org/10.1364/BOE.484257
Received 22 Dec 2022; accepted 6 Jan 2023; published 26 Jan 2023

imaging system [11]. In the past, significant effort has been made to measure transverse flow with OCT. One method proposed the use of the variance of the temporal Doppler to determine the lateral flow velocity component [11]. Multi-angle Doppler OCT has been developed for reconstruction of the 3D flow velocity using Doppler signals from multiple angles [13–15]. However, it requires precise prior knowledge of the incident angle, and the calibration process could be cumbersome. Recently, digital sub-aperture based (DSubAp) Doppler OCT has been proposed. This approach calculates the lateral flow motion based on the phase differences between digitally reconstructed OCT tomograms corresponding to different sub-apertures [16,17]. Since DSubAp DOCT requires excellent lateral phase stability of the acquired OCT volumes, this method is usually applied to parallelized imaging modalities such as full-field (FF) swept-source (SS) OCT or line-scan (LS) spectral-domain (SD) OCT. FF SS-OCT offers volumetric acquisition rates in the order of 100 to 200 Hz, therefore its flow speed detection range is very limited. LS SD-OCT only maintains excellent phase stability along the parallel illumination direction; therefore, it can only determine the velocity along the line illumination direction. Since the wave vector's axial component is much larger than the transverse one, even low axial velocity can result in ambiguity because of phase wrapping in LS SD-OCT.

DLS analyzes the temporal fluctuations of the scattering signals and was originally used to measure the particle size distributions [18]. Recently, DLS has been used to measure blood flow dynamics using different imaging techniques [19–21]. Here, we limit our discussion to OCT-based studies. The combination of DLS and time-domain (TD) OCT was originally developed for studying Brownian motion in scattering media [22–24]. Afterwards, flow velocity detection was demonstrated with combination of DLS and Fourier-domain (FD) OCT [9]. DLS-OCT can resolve axial and lateral velocities with single-beam point-scanning OCT modality with first-order or second-order autocorrelation of the temporal OCT signal [11,25–27]. DLS-OCT requires ultrahigh temporal sampling of the autocorrelation function, therefore, most studies applied repeated A-scans, which typically takes several minutes for acquiring a 3D dataset [9]. Multiple studies have attempted to resolve flow dynamics by recording repeated B-scans instead of A-scans [20,28,29]; however, the flow velocity detection range is very limited due to the extremely restricted time resolution.

Here, we present a novel decorrelation-based method for measuring localized transverse flow using LS SD-OCT technology, named DLS-LS-OCT in this work. First, we theoretically verified the DLS-OCT model for a LS-OCT configuration. Then, we developed a novel method for determining the transverse flow velocity along the line-illuminating direction by comparing the autocorrelation functions of the original and digitally generated low-resolution OCT tomograms. Next, the novel DLS-LS-OCT method was validated by imaging intralipid flow in a glass capillary phantom. Last, we used a microfluidic device to demonstrate that the DLS-LS-OCT method can be used to map the spatial distribution of the flow velocity in the line-beam illumination plane.

2. Theory

2.1. Temporal autocorrelation of the LS SD-OCT signal

In this work, x-direction is defined as the scanning direction of the LS SD-OCT system, z-direction is defined as the light propagation direction, and y-direction is defined as the direction orthogonal to the xz-plane. Location (x, y, z) represents the center position of the optical volume under study. The LS SD-OCT's complex-valued signal of N discrete point scatters can be written as (see Supplement 1):

$$f(x,y,z) = \sum_{j=1}^{\mathrm{N}} e^{i2nk_0 z_j} e^{-2\frac{x_j^2}{\sigma_x^2 + i\frac{2z_j}{k_0}}} e^{-\frac{y_j^2}{\sigma_y^2 + i\frac{2z_j}{k_0}}} e^{-\frac{z_j^2}{\sigma_z^2}} \tag{1}$$

where (x_j, y_j, z_j) is the Cartesian coordinate of the jth scatter, $\sigma_{x,y}$ is the 1/e transverse beam waist radius of the coherent point spread function (PSF) of the detection optics along the x- and y-direction, and σ_z denotes the 1/e radius of the axial PSF. We have assumed that the axial and lateral point spread functions follow Gaussian distribution. The $e^{i2\mathrm{n}k_0 z_i}$ represent the optical path delay, ${\sigma^2}_{x,y} + i2z_i/k_0$ describes the defocus, and the factor of 2 difference of the x- and y-direction is related to the design of the LS SD-OCT system which results in a confocal configuration in the x-direction and a wide-field configuration in the y-direction.

The normalized first order temporal autocorrelation function of the LS SD-OCT signal can be expressed as (Supplement 1):

$$\hat{g}_1(t) = \frac{g_1(t)}{g_1(0)} = e^{i2nk_0 v_z t} e^{-4n^2 k_0^2 D t} e^{-(\frac{v_x^2}{\sigma_x^2} + \frac{v_y^2}{2\sigma_y^2} + \frac{v_z^2}{2\sigma_z^2})t^2} \tag{2}$$

where $g_1(t) = \langle f(x, y, z, t) f(x, y, z, 0)^* \rangle$, t denotes the autocorrelation time delay, $v_{x,y,z}$ represents the scatters' translational velocity, and D is the diffusion coefficient of the scatters. The derived first-order temporal autocorrelation of OCT signal in LS SD-OCT is similar to that of a point-scanning OCT modality [30]. However, it is important to note that there are two main differences between the two modalities: (1) the transverse resolution of the LS SD-OCT system in the x- and y- directions are not the same since this modality has a confocal configuration in the x-direction and a wide-field configuration in the y-direction. (2) The LS SD-OCT's time resolution is lower than that of point-scanning OCT since LS SD-OCT records all A-scans in a B-scan in parallel, therefore its time resolution is actually the time interval between adjacent B-scans while point-scanning OCT technology uses M-mode scanning which acquires repeated A-scans.

2.2. Noise influence on the autocorrelation function

So far, we have considered only the autocorrelation of the noise-free OCT signal. By assuming the noise is a stochastic zero-mean complex Gaussian variable, the normalized autocorrelation function under noise can be expressed as [31,32]:

$$\tilde{g}_1(t) = \gamma \hat{g}_1(t) \tag{3}$$

where $\gamma = 1 \Big/ \left(1 + \frac{\langle |n|^2 \rangle}{\langle |s|^2 \rangle}\right)$ and s and n denote the actual OCT signal and noise respectively. The noise contributes to additional decay of the autocorrelation function by multiplying a correction ratio which is independent of time; thus, the decay rate does not change with or without noise. Since the OCT signal and noise are both position-dependent, the correction ratio γ is also a function of the spatial position. In point-scanning imaging modalities, the noise is assumed to be dominated by the shot noise of the reference signal and can be compensated with pre-recorded reference arm noise [32]. However, when LS SD-OCT technology is used for imaging scattering media, multiply scattered light is detected because of the wide-field configuration along its line illumination direction, particularly at greater imaging depths. Therefore, it is incorrect to assume that the noise is independent on the detected scattered light.

2.3. DLS-LS-OCT

Currently, the two often used methods for determining flow velocity in DLS-OCT are: (1) fitting the autocorrelation function directly to determine the diffusion rate and flow velocity simultaneously [33]; (2) calculating the flow velocity based on the bandwidth of the power spectrum density of the autocorrelation function [11]. The first method can be very precise when the time resolution is high enough, so that there is sufficient autocorrelation data above the noise floor. The second method is commonly used in cases where the translational motion is predominant such that the diffusion effect is negligible. Since the time resolution of the current version of the LS SD-OCT system (0.34 ms) is significantly lower than the time resolution of a point-scanning OCT modality when operated in M-scan mode (typically 20 μs or smaller), the autocorrelation function reaches the noise floor fast even at low velocity. As a result, it is not possible to apply those methods directly. However, it is possible to calculate the diffusion coefficient in the absence of flow and fit the translational velocity with the diffusion compensated autocorrelation function. Unfortunately, this approach is not precise, as will be shown in the "Results" section.

To overcome these difficulties, a low-resolution tomogram is generated digitally, taking advantage of the high phase stability of each B-scan. The Fourier translation of OCT signal along y-direction is:

$$f(x,k_y,z) = \sum_{j=1}^{N} e^{i2nk_0 z_j} e^{-2\frac{x_j^2}{\sigma_x^2 + i\frac{2z_j}{k_0}}} e^{-\frac{z_j^2}{\sigma_z^2}} (e^{-\frac{\sigma_y^2 + i\frac{2z_j}{k_0}}{4} k_y^2} e^{ik_y y_j}) \tag{4}$$

The low-resolution OCT signal can be generated by inverse Fourier transforming the product of $f(x,k_y,z)$ and a Gaussian filter $e^{-\frac{m^2}{4}k_y^2}$:

$$\begin{aligned} f'(x,y,z) &= IFT_{k_y \rightarrow y}\{\sum_{j=1}^{N} e^{i2nk_0 z_j} e^{-2\frac{x_j^2}{\sigma_x^2 + i\frac{2z_j}{k_0}}} e^{-\frac{z_j^2}{\sigma_z^2}} [(e^{-\frac{\sigma_y^2 + i\frac{2z_j}{k_0}}{4} k_y^2} e^{ik_y y_j}) e^{-\frac{m^2}{4}k_y^2}]\} \\ &= \sum_{j=1}^{N} e^{i2nk_0 z_j} e^{-2\frac{x_j^2}{\sigma_x^2 + i\frac{2z_j}{k_0}}} e^{-\frac{y_j^2}{\sigma_y'^2 + i\frac{2z_j}{k_0}}} e^{-\frac{z_j^2}{\sigma_z^2}} \end{aligned} \tag{5}$$

where $\sigma_y{}' = \sqrt{\sigma_y^2 + m^2}$ is the reduced resolution along the y-direction. Follow the same derivation, the autocorrelation function of the low-resolution OCT signal under noise is:

$$\tilde{g}_1'(t) = \gamma' e^{i2nk_0 v_z t} e^{-4n^2 k_0^2 D t} e^{-(\frac{v_x^2}{\sigma_x^2} + \frac{v_y^2}{2\sigma_y'^2} + \frac{v_z^2}{2\sigma_z^2})t^2} \tag{6}$$

With the assumption that the two noise correction ratios are the same, the ratio of the two autocorrelation functions is:

$$G_1(n\tau) = \frac{\tilde{g}_1(\mathrm{n}\tau)}{\tilde{g}_1'(\mathrm{n}\tau)} = e^{-(\frac{1}{2\sigma_y^2} - \frac{1}{2\sigma_y^2})v_y^2 \mathrm{n}^2 \tau^2} \tag{7}$$

where n is the number of time steps and τ is the time resolution. Here we drop the continuous representation and use a discrete representation since the obtained autocorrelation function is discrete. Since G_1 is independent with the noise correction coefficient, the diffusion rate, and the translational velocity components v_x and v_z, the speed along the y-direction, v_y can be calculated as:

$$v_y = \frac{1}{\mathrm{n}\tau}\sqrt{2\ln|G_1(\mathrm{n}\tau)|\frac{\sigma_y'^2 \sigma_y^2}{\sigma_y'^2 - \sigma_y^2}} \tag{8}$$

In practice, the two noise correction ratios, γ and γ', may not be the same since the effect of the Gaussian filter can be different for the signal and the noise. Therefore, calculating v_y using a single time delay might be not accurate. Instead, more time delays should be used to get rid of the noise correction ratio influence (see section 3.5).

3. Methods

3.1. LS SD-OCT system and sample preparation

The experimental procedures described here were carried out using a LS SD-OCT system reported recently [34] that was modified slightly. The schematic of the system is shown in Fig. 1(A). The system is based on a free-space Michelson interferometer and is powered by a supercontinuum laser (SuperK, NKT Photonics, Birkerød, Denmark). A customized band-pass filter was utilized to select a spectral range of 600 nm ~ 980 nm. The line illumination is generated using a cylindrical lens. An infinity-corrected 5x microscope objective (M Plan NIR, Mitutoyo, Japan) was used, and the current optical design of the LS SD-OCT system resulted in lateral resolution of ~4 μm (Fig. 1(B)). A narrow Gaussian filter was applied on the spectrum in post-processing to ensure that the autocorrelation signal is consistent with the theory and to reduce the influence of the axial velocity on the autocorrelation function. The detected spectrum after the digital filtering is centered at 800 nm with spectral bandwidth of about 50 nm measured at full width at maximum half (FWMH). The theoretical axial resolution in free space is 5.6 μm, which is consistent with the experimental result of 5.5 μm (Fig. 1(C)). The optical power incident on the imaged object was 2.0 mW, however, the effective power is lower considering the digital Gaussian filter applied. The effective SNR was ~83 dB at the center of the line illumination and ~73 dB at the edges because of the Gaussian intensity distribution of the line illumination. The interference signal is detected by a 2D CMOS camera (Dimax S4, PCO, Germany) with a detection area of 1920 × 500 pixels (spectral × spatial) and data was acquired at the rate of 2,946 fps, equivalent to a time resolution of $\tau = 0.34$ ms. Only the central 300 A-scans were used for the velocity analysis due to the low SNR at the B-scan edges.

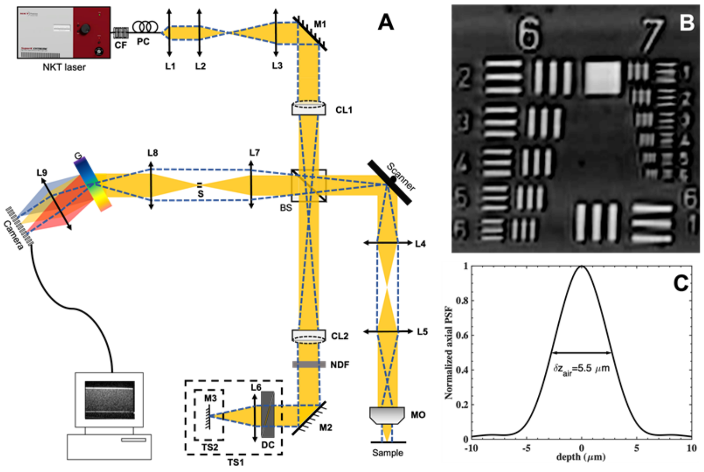

Fig. 1. (A) Schematic of the LS-SD-OCT system. Scanning (x) and parallel (y) directions of the optical beam are represented by the solid yellow color and the blue dashed line respectively. (B) Enface image of an USAF 1951 resolution target (groups 6 and 7). (C) Normalized axial PSF after software dispersion compensation. BS, non-polarizing beam splitter; CF, customized filter unit; CL, cylindrical lens; DC, dispersion compensator; G, transmission grating; L, lens; M, mirror; MO, microscope objective; NDF, neutral density filter; PC, polarization controller; S, slit aperture; TS, translational stage.

Flow measurements were conducted in two flow phantoms: a glass capillary and a microfluidic device. Diluted 5% intralipid was pumped with a single syringe pump (NE300, Pump System Inc) into the glass capillary phantom (QGCT0.2, Capillary Tube Supplies Ltd) or the custom polydimethylsiloxane (PDMS) microfluidic device [35]. Flow rates were set at 0, 0.6, 1.2, 1.8, and 2.4 μL/min for the glass capillary and 7.5 μL/min for the microfluidic device. A total of 800 repeated B-scans were recorded at the same location.

3.2. Axial phase correction

Due to inevitable axial motion, such as mechanical vibration of the phantom's support stage, the OCT signal's phase information is distorted and results in measurement of incorrect Doppler phase shifts and autocorrelation function. Since this additional axial displacement between adjacent B-scans is in the sub-micron range, the bulk motion-induced phase error $\Delta\phi$ can be compensated. Since the B-scan of the same scanning location (x-direction) is collected repeatedly, the OCT signal is rewritten as:

$$f(\mathrm{n}\tau, y, z) = A(\mathrm{n}\tau, y, z)e^{i\phi(\mathrm{n}\tau,y,z)}, \mathrm{n} = 1, 2, 3\ldots, \mathrm{N} \tag{9}$$

where n refers to the n^{th} B-scan signal, N is the total number of B-scans, and τ is the time resolution of the LS SD-OCT system. Because of the parallel imaging configuration of LS SD-OCT and the fast frame rate, it can be assumed that the bulk axial translations of all the A-scans within the same B-scan are the same [36]. The weighted averaged phase difference of two adjacent B-scans is:

$$\Delta\phi_{\mathrm{n}} = \arg[\sum_{(y,z)\in D} f(\mathrm{n}\tau, y, z)f((\mathrm{n}+1)\tau, y, z)^*], \mathrm{n} = 1, 2, 3\ldots, \mathrm{N}-1 \tag{10}$$

where D is a user-selected static region without translational flow and the asterisk denotes the complex conjugate. The accumulated axial bulk motion-induced phase difference of the nth B-scan with respect to the first B-scan is:

$$\Delta\Phi_{\mathrm{n}} = \sum_{i=1}^{\mathrm{n}-1} \Delta\phi_i, \mathrm{n} = 2, 3, 4\ldots, \mathrm{N} \tag{11}$$

The OCT signal is then corrected by multiplying with a phasor:

$$f_{\mathrm{corr}}(\mathrm{n}\tau, y, z) = f(\mathrm{n}\tau, y, z)e^{i\Delta\Phi\mathrm{n}} \tag{12}$$

3.3. Digital sub-aperture-based Doppler OCT

We used the digital sub-aperture-based Doppler (DSubAp) OCT method repeated in [16,17] with small modification. Two symmetric sub-apertures, $[-k_{y,c} - \delta k_y/2, -k_{y,c} + \delta k_y/2]$ and $[k_{y,c} - \delta k_y/2, k_{y,c} + \delta k_y/2]$, are used to filter out the sub-aperture signals $f_{\mathrm{corr,l}}(\mathrm{n}\tau, k_y, z)$ and $f_{\mathrm{corr,r}}(\mathrm{n}\tau, k_y, z)$. Here, $\pm k_{y,c}$ and δk_y refer to the centers and size of the two sub-apertures. In this study, we confined the sub-aperture size to be 1/10 of the full aperture $\delta k_y = \Delta k_y/10$, and the centers of the two sub-apertures are set to $\pm k_{y,c} = \pm\Delta k_y/4$.

Although the small sub-aperture leads to smaller signal SNR thus higher phase noise, averaging the phase difference N − 1 times can improve the accuracy as N is in the order of several hundred in this study:

$$\begin{aligned} \delta\phi_{\mathrm{l}}(y, z) &= \arg[\sum_{\mathrm{n}=1}^{\mathrm{N}-1} f_{\mathrm{corr,l}}(\mathrm{n}\tau, y, z)f_{\mathrm{corr,l}}((\mathrm{n}+1)\tau, y, z)^*] \\ \delta\phi_{\mathrm{r}}(y, z) &= \arg[\sum_{\mathrm{n}=1}^{\mathrm{N}-1} f_{\mathrm{corr,r}}(\mathrm{n}\tau, y, z)f_{\mathrm{corr,r}}((\mathrm{n}+1)\tau, y, z)^*] \end{aligned} \tag{13}$$

The velocity along y-direction can be rewritten as (see Supplement 1):

$$v_y = \frac{\delta y}{\pi\tau}[\delta\phi_{\mathrm{r}}(y, z) - \delta\phi_{\mathrm{l}}(y, z)] \tag{14}$$

where δy is the digital resolution of the LS-OCT system. It has been pointed out that when the scatters are out of focus, the axial motion gradient induces additional phase change that can be misinterpreted as lateral motions [16,37]. Since digital refocusing of the flow signal is challenging because of the lack of distinguishable structures in the phantoms, we use DSubAp DOCT as a gold standard only when there is no axial motion.

3.4. DLS-LS-OCT

According to the Wiener–Khinchin theorem, the 1st order autocorrelation of a function is the Fourier transform of its power spectral density (PSD). The temporal autocorrelation of the axial phase corrected OCT signal can be calculated more efficiently using its PSD than following the definition:

$$g_1(t) = IFT_{\omega\to t}\{|FT_{t\to\omega}\{f_{\mathrm{corr}}(t,y,z)\}|^2\} \tag{15}$$

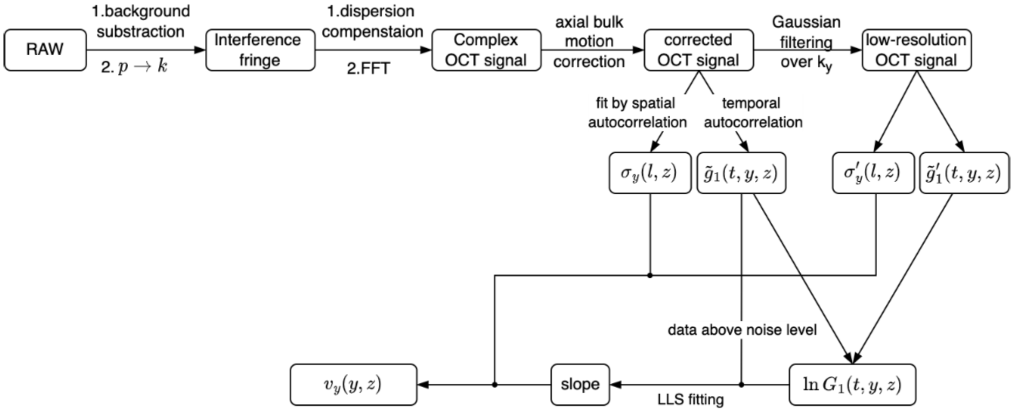

Fig. 2. Flow chart for the proposed method.

The normalized autocorrelation function is thus $\tilde{g}_1(t) = \frac{g_1(t)}{g_1(0)}$.

A low-resolution OCT signal is generated by applying a Gaussian filter to the transverse spatial frequency distribution function of the original OCT dataset, followed by inverse Fourier transforming back to spatial space:

$$f'_{\mathrm{corr}}(\mathrm{n}\tau,y,z) = IFT_{k_y\to y}\{FT_{y\to k_y}\{f_{\mathrm{corr}}(\mathrm{n}\tau,y,z)\}\times\exp(-\frac{2k_y^2}{(a\varDelta k_y)^2})\} \tag{16}$$

where a controls the size of the applied Gaussian filter, and $\varDelta k_y$ is the full bandwidth of the transverse spatial frequency. In this study, the size of the filter is set as $a = \frac{1}{4}$ as a compromise of the resolution reduction and translational motion induced decay contrast.

Once the localized resolutions σ_y and σ'_y are determined, the velocity component v_y, in principle, can be calculated following Eq. (8). The result is supposed to be independent on the time delay, as long as $\tilde{g}_1(\mathrm{n}\tau)$ is above the noise floor. However, we find that the results using different time lags differ from the gold standard to some extent. Thus, linear least squared (LLS) fitting is performed on all time delay steps at which $\tilde{g}_1(\mathrm{n}\tau)$ is above a user-selected threshold. If the noise correction ratios of the original and low-resolution tomograms slightly differ, Eq. (7) should be corrected as:

$$G_1(\mathrm{n}\tau) = \tilde{\gamma}e^{-(\frac{1}{2\sigma_y^2}-\frac{1}{2\sigma_y'^2})v_y^2\mathrm{n}^2\tau^2} \tag{17}$$

where $\tilde{\gamma} = \frac{\gamma}{\gamma'}$ is an unknown factor that can be get rid of by taking the logarithm of both sides:

$$\ln[G_1(n\tau)] = \ln[\tilde{\gamma}] - (\frac{1}{2\sigma_y^2} - \frac{1}{2\sigma_y'^2})v_y^2\tau^2\mathrm{n}^2 \tag{18}$$

As it can be seen, $\ln[G_1(n\tau)]$ is a linear function of n^2. Once the linear slope η is fitted, the v_y can be calculated using the following formula:

$$v_y = \frac{1}{\tau}\sqrt{2|\eta|/(\frac{1}{\sigma_y^2} - \frac{1}{\sigma_y'^2})} \tag{19}$$

In this work, n = 1, 2, . . . , m − 1, where m is the first time-delay point at which $\tilde{g}_1(\mathrm{n}\tau)<0.15$ and is confined in the range of [3, 15]. The data processing steps of DLS-LS-OCT are presented in Fig. 2.

3.5. Localized resolution

The depth-resolved resolution parameters, $\sigma_y(z)$ and $\sigma_y'(z)$ can be measured using the spatial autocorrelation of the B-scan signal in terms of lateral shift [32]. Considering the resolution across the lateral direction can be different, we evenly divide each B-scan into 12 columns and determined $\sigma_y(l, z)$ and $\sigma_y'(l,\ z)$ of each column separately (see Supplement 1).

4. Results

4.1. Validation of DLS-LS-OCT performance without axial velocity gradient

In this experiment, we evaluated the performance of the DLS-LS-OCT without axial velocity gradient. We start by determining the localized transverse resolution parameters, $\sigma_y(z)$ and $\sigma_y'(z)$, based on the spatial (y-direction) autocorrelation of the B-scan signal. Figure 3 shows the measurement of the localized resolution parameters of the diluted intralipid at a flow rate of 2.4 uL/min. As shown in Fig. 3(A), the glass capillary was placed parallel to the beam illumination plane and perpendicular to the beam propagation direction to ensure the flow velocity is along the y-direction. The illumination plane is slightly mismatched with the center of the glass capillary to avoid self-interference and signal saturation from the glass capillary walls. Figure 3(B) shows a typical log-scale B-scan image of the flow phantom. The red box indicates the selected region of interest (ROI), which is the 7th column of the 12 evenly divided areas. The axial position of the glass capillary was set ~ 50 μm away from the location at which the top glass-intralipid interface's signal was at its maximum. The laterally averaged OCT signal attenuates rapidly from the top to the bottom due to beam defocusing and light scattering in the intralipid, leading to higher uncertainties for both phase-based and autocorrelation-based flow speed measurements. As it can be seen, there were some artifact signals in the bottom intralipid-to-glass interface and under the glass-air interface which are due to multiple scattering in the intralipid. Figure 3(C) shows the original and the digitally generated low-resolution enface images of a microsphere. The blue and red lines mark the locations for the with the Y-direction intensity analysis which are displayed in Fig. 3(D). The depth-resolved resolution parameters of the selected ROI are shown in Fig. 3(E). The blue and orange lines represent the resolution parameters along the y-direction of the original and digitally generated low-resolution OCT images respectively. The 2 peaks correspond to the 2 glass-intralipid interfaces. As expected, the resolution parameters of the scattering intralipid are larger than those of the noise and smaller than those of the diffuse reflection from the interfaces. This is because the estimated resolution parameters are negatively correlated with the autocorrelation function. The resolution of the scattering sample was reported to be independent of the position [30,33]. However, our result shows that the resolution parameters at the bottom of the sample are slightly smaller than those at the top. This might be due to the fact that the low SNR and accumulated multi-scattering at the bottom region result in additional decorrelation.

Once the $\sigma_y(z)$ and $\sigma_y'(z)$ are determined, we can calculate the transverse velocity v_y following the methods described in section 3.5. Figure 4(A) shows the autocorrelation at different time delay steps ($\mathrm{n}\tau$) as a function of depth. The solid line indicates the normalized autocorrelation of

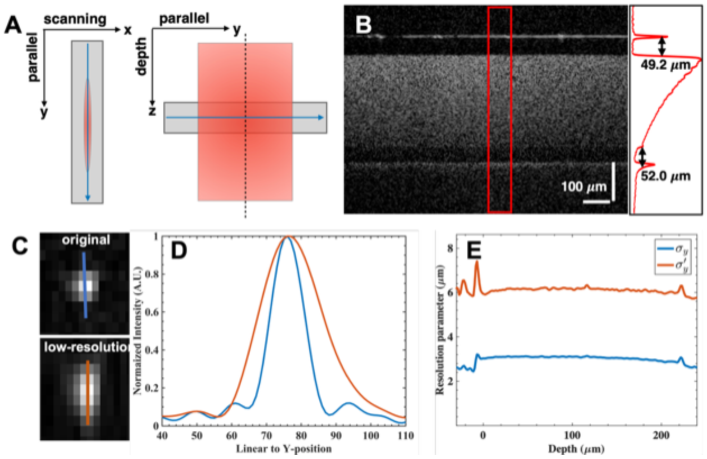

Fig. 3. Measurement of the localized resolution parameters of the diluted intralipid at a flow rate of 2.4 *u*L/min. (A) Schematic of the flow orientation. (B) A typical log-scale B-scan image of the flow capillary with the signal amplitude attenuation analysis. The red box indicates the selected region of interest (ROI) within which the signal amplitude and localized resolutions are analyzed. (C) Original and low-resolution enface images of a microsphere. The blue and red lines mark the locations for the with the Y-direction intensity analysis which are displayed in Fig. 3(D). The estimated localized resolution parameters, $\sigma_y(z)$ (blue) and $\sigma'_y(z)$ (orange) are shown in Fig. 3(E).

the original OCT signal $\tilde{g}_1$ and the dashed line represents the ratio of the autocorrelations of the original and low-resolution signal $G_1 = \tilde{g}_1/\tilde{g}_1{}'$. Both $\tilde{g}_1$ and G_1 were averaged along y-direction within the selected ROI shown in Fig. 3(B). If there is no noise, the autocorrelation decays $\tilde{g}_1(\mathrm{n}\tau)$ with the same translational velocity are supposed to be the same. Since the speed distribution $v_y(z)$ of the laminar flow in a circular pipe is parabolic, the noise-free autocorrelation $\hat{g}_1(\mathrm{n}\tau, z)$ should be spatially symmetric. However, the noise breaks this symmetry, as shown by the solid lines. The noise influence on the autocorrelation function is modeled as a linear correction ratio which is dependent on the SNR [31,32]. In our proposed method, both autocorrelation $\tilde{g}_1(\mathrm{n}\tau, z)$ and $\tilde{g}'_1(\mathrm{n}\tau, z)$ suffer similar, if not the same, reduction such their ratio, $G_1(\mathrm{n}\tau, z)$, recovers the spatial symmetry, which is shown by the dash line. In the depth range $z \in (60, 170)\mu$m, $G_1(4\tau, z)$ shows randomly oscillations because $\tilde{g}_1(4\tau, z)$ reaches the noise level.

It is worth noting that the ratio $G_1(\mathrm{n}\tau, z)$ is supposed to be 1 at the depth of 0 μm at which the translational speed is 0. However, $G(\mathrm{n}\tau, 0)$ is lower than 1, as indicated by the black arrow in Fig. 4(A). This might be due to the fact that reflection from the glass-intralipid interface breaks the single scattering assumption. The noise-free upper flow speed detection limit for can be estimated as follows. For the LLS fitting method, since at least two time-delay steps are required, the n = 2 lines are used. The solid line shows that the diffusion decay term at $t = 2\tau$ is about 0.74 since the SNR at depth 0 μm is high and the noise correction ratio is negligible. The dashed line indicates the translational motion decay term $\exp\left(-\frac{4\tau^2 v_y^2}{\sigma_y^2}\right)$ is estimated as 0.54 at a speed of 3.5 mm/s, using the average resolution parameters determined in Fig. 3(D) and assuming the noise correction ratios are the same. Thus, v_y can increase to 6.3 mm/s at which $g_1(2\tau)$ reaches the noise level of 0.1. Similarly, the upper limit using a single time decay step is 13.5 mm/s. In practice, due to the presence of noise, the maximum detectable flow speed can be smaller than the upper limit. Figure 4(B) shows the plot of $\tilde{g}_1(\mathrm{n}\tau)$ at 4 different depths, at which all the autocorrelation functions decay into the noise floor within 5 time-delay steps. Since the effect of

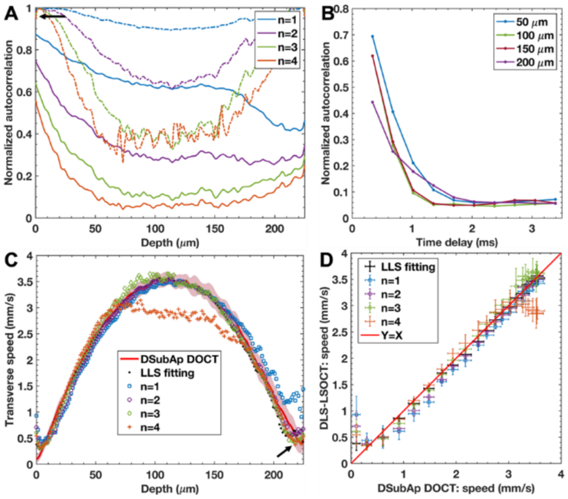

Fig. 4. Comparison of the DLS-LS-OCT results determined by single time delay and linear least squared (LLS) fitting. The dataset is the same as that used for the results shown in Fig. 3. (A) Autocorrelation at different time delay steps ($n\tau$) as a function of depth. The solid line and dashed line indicate the autocorrelation function of the original OCT signal $\tilde{g}_1$ and the ratio of the autocorrelation of the original and low-resolution signal $G_1 = \tilde{g}_1/\tilde{g}_1{}'$, respectively. (B) Autocorrelation of the original OCT signal $\tilde{g}_1(n\tau)$ at depth 50 μm, 100 μm, 150 μm, and 200 μm. (C) Measured transverse flow velocity v_y as a function of depth. The scatter plots are the results of DLS-LS-OCT using LLS fitting and different time delay steps. The result of digital sub-aperture-based (DSubAp) DOCT is indicated by the red line and its 3-sigma uncertainty is shown by the red-with-opacity area. (D) Speed comparison measured by DLS-LS-OCT and DSubAp DOCT at different depths. $z \in (0, 110)$ µm. The red line indicates the reference at which the 2 measured speeds are equal.

the noise on the autocorrelation function is SNR dependent, the $\tilde{g}_1(n\tau)$ measured at depths 100 μm and 150 μm is almost indistinguishable despite the fact that the translational velocities at these two depths are different. This implies that the estimation of the flow velocity based on $\tilde{g}_1$ alone when measured with LS SD-OCT modality is not reliable. Figure 4(C) shows comparison of the flow velocity results of the DLS-LS-OCT method estimated by LLS fitting with different time delay steps. The flow speed and its 3-sigma uncertainty determined by DSubAp DOCT are shown by the red line and red-with-opacity area. It has been proven theoretically that the DSubAp DOCT result is distorted when the axial velocity gradient and defocus aberration exist simultaneously [37]. Nevertheless, since there was no translational velocity in z-direction in this experiment, the reported distortion should not exist and the averaged DSubAp DOCT result can be used as a gold standard. In the range $z \in (60, 170)$ μm, there is a significant difference between the speed estimated by $G_1(4\tau, z)$ and the reference speed as $\tilde{g}_1(4\tau, z)$ is overwhelmed by the noise. In order to provide a quantitative correlation of the results of the DLS-LS-OCT and the gold-standard reference, we define the fidelity of the two results as:

$$F = 1 - \frac{\sum_i |v_y(z_i) - v_{y,r}(z_i)|}{\sum_i |v_{y,r}(z_i)|} \tag{20}$$

where $z_i \in (0, 110)\mu$m. The bottom half area is excluded since the phase of the OCT signal acquires an additional change due to multi-scattering thus the speed distortion at the bottom is larger than at the top. One evidence for this effect is that at the bottom intralipid-glass interface, where translational motion does not exist, the result of DSubAp DOCT is well above 0, as indicated by the blue arrow. The fidelities of the results determined by LLS fitting and single time delay steps (n = 1, 2, 3, 4) are 0.980, 0.933, 0.961, 0.959, and 0.906 respectively. Figure 4(D) shows the speed comparison measured by DLS-LS-OCT and DSubAp DOCT at different depths. Data is acquired at every 4 steps from depth 0 to 110 μm and the LLS result (black dots) provides an excellent fit to the ground truth (red line). One possible explanation for the better performance of the LLS fitting method is that the noise correction ratio γ is not exactly the same for the original and the low-resolution OCT datasets, such that the single time delay step method cannot completely compensate for it. In the following study, the LLS fitting method is used unless stated otherwise.

Figure 5 shows comparison of the performance of the proposed DLS-LS-OCT method with the two other DLS-OCT based methods: (i) determine v_y using the bandwidth of the power spectral density (PSD) of the temporal B-scan signal (see Supplement 1); (ii) compensate the diffusion term with diffusion coefficient determined at zero flow rate (see Supplement 1). Figure 5(A) shows the OCT signal's power spectral density $s(\omega, z)$ of the selected ROI in Fig. 3(B). Since there is no translational motion in the axial direction, the center of the Doppler signal distribution was located at the 0 frequency. The blue and red lines in Fig. 5(B) indicate the depths at which the power spectral density was fitted with a Gaussian distribution. The bandwidth of the fitted curve is used to calculate the flow speed, as shown in Fig. 5(E). The diffusion coefficient of the diluted intralipid is determined without translational motion. The intralipid's OCT signal is evenly divided into 30 × 24 ($x \times z$) blocks and the temporal autocorrelation is averaged within each block before fitted with model $\tilde{g}_1(t) = \gamma e^{-4n^2k_c^2Dt} + b$. Figure 5(C) shows the mean value and standard deviation of the diffusion coefficient at different depths. A typical fitting of the $|\tilde{g}_1(\tau)\rangle$ averaged within one block is displayed in Fig. 5(D). The diffusion coefficient of the intralipid averaged over all the blocks is 1.56 ± 0.02 μm^2/s. Figure 5 (E) and (F) compare the transverse speeds estimated by DLS-LS-OCT, DLS-OCT power spectral density (PSD), and DLS-OCT diffusion compensation (DC). The results are first calculated using the laterally averaged temporal autocorrelation within the 12 sub-tomograms and then averaged over the sub-tomograms. Only the DLS-LS-OCT results show good correlation with the "gold standard". The DLS-OCT PSD method does not agree with the reference speed since it does not take the diffusion effect into consideration.

In the case where the flow speed is high and the particle size is large, the diffusional decay is usually ignored since the translational decay dominates. However, in this experiment these two decays are comparable. For instance, at the first time delay step, the decays due to the diffusional and translational motion are 0.79 and 0.85 respectively, estimated using the averaged diffusion rate D = 1.56 μm^2/s, the resolution parameter $\sigma_y = 2.15$ μm, and a translational flow speed of 3.5 mm/s. It has been reported that due to the diffusional motion, the power spectral density has a Lorentzian line shape instead of a delta function when the flow rate is set to zero [22–24,38]. This explains why the estimated speed is larger than 0 near the top glass-intralipid interface. In fact, the speed estimated by DLS-OCT PSD is a parameter describing any dynamics of the scatterers in the imaged object, and it is not a true measure of the translational velocity. The DLS-OCT DC result is not precise as well. One possible reason is that the estimated diffusion coefficient is not accurate. The model, Eq (2), assumes a 180° scattering angle which is not always valid for the case of scattered light detected with a microscope objective with NA = 0.15. This can be improved by using an imaging probe with smaller effective NA, however, the impact of translational velocity on the autocorrelation function is reduced due to the larger beam waist, leading to a reduced sensitivity to low velocity motion. Since the particle size of the intralipid suspension is not uniform, the measured diffusion coefficient is an ensemble average over the contribution of particle sizes. For example, it has been shown by transmission electron microscopy that the diameter of intralipid particles varies from 20 nm to 700 nm [39]. Another

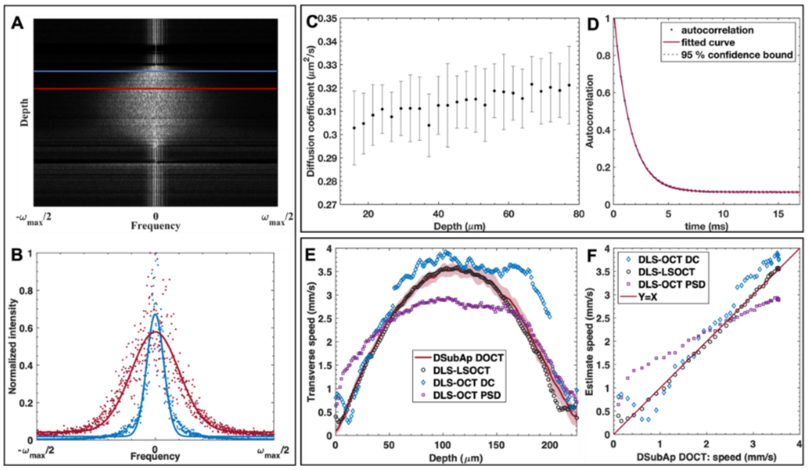

Fig. 5. Comparison of the transverse speed determined by DLS-LS-OCT, DLS-OCT PSD, and DLS-OCT DC. The dataset is the same as that of Fig. 3. (A) Depth resolved power spectral density $s(\omega, z)$ of the ROI selected in Fig. 3. (B) Scatter plots and the fitted Gaussian curves of the power spectral density at depths labeled by the blue and red lines in (A). (C) Diffusion coefficient measured in the absence of flow. (D) A typical averaged autocorrelation $\tilde{g}_1(\tau)$ and its fitted curve. The dash line shows the 95% confident bound. (E) Transverse flow velocity v_y as a function of depth. The scatter plots show the results determined by DLS-LS-OCT, DLS-OCT power spectral density (PSD), and DLS-OCT diffusion compensation (DC). The DSubAp DOCT result is shown as the “gold standard” reference. (F) Speed comparison measured by DLS methods and DSubAp DOCT at different depths.

factor leading to the inaccurate results of the DLS-OCT DC method is that the noise-induced ratio correction model might not be valid when the SNR is low, especially in the presence of multiple scattering.

Figure 6 shows a comprehensive comparison of the DLS-LS-OCT and DSubAp DOCT performance without axial velocity. Figure 6(A) and (B) show the localized transverse speed $v_y(y, z)$ of the B-scan estimated by the DSubAp DOCT and DLS-LS-OCT methods respectively. Both speed distribution maps suggest that the transverse speed of the intralipid flow is parabolically distributed along the z-direction and is constant along the y-direction. The two results match very well except for 4 differences. (1) The large-size speckle pattern in Fig. 6(A) indicates poor lateral resolution due to the small sub-apertures utilized in DSubAp DOCT. Also, the speed distribution map in Fig. 6(A) is smoother than in Fig. 6(B). This is because the result from DSubAp DOCT is an average of the 799 adjacent B-scan pairs’ results, while the result from DLS-LS-OCT is only fitted once though the temporal autocorrelation is determined based on 800 repeated B-scans. (2) The noise in the air and glass regions in Fig. 6(B) suggests that the DLS-LS-OCT is not robust when there is no scattering or reflected signal. The fast decorrelation of the noise is interpreted as a high speed thus a binary mask generated by the OCT or OCTA image is needed to block the noise-only regions. (3) The white arrow in Fig. 6(A) shows a fake speed signal located at the bottom glass-air interface resulting from the additional phase change signal associated with detection of the multiply scattered light. The fake speed signal also appears at the same location in Fig. 6 (B) though its value is smaller. The possible causes for the fake signal in DLS-LS-OCT include mechanical vibrations, inaccurate resolution parameters because of the reflecting (Fig. 3(D)), and low SNR. Further investigation is required to determine how multiply scattered light contributes to the generation of the fake speed signal. (4) The red

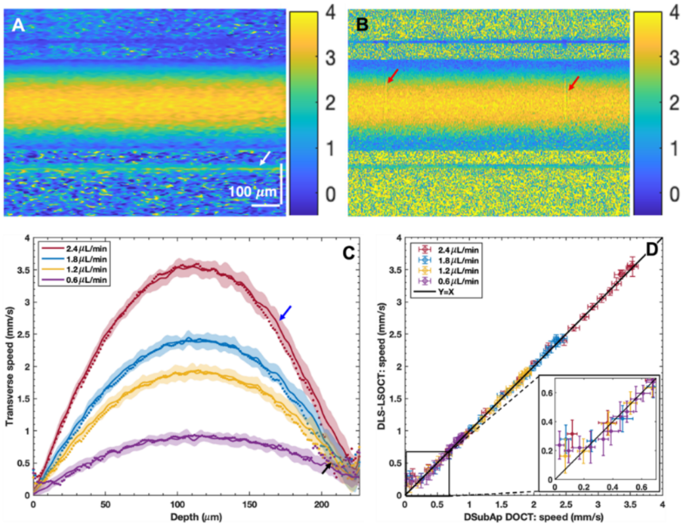

Fig. 6. Comparison of the localized transverse speed determined by DSubAp DOCT and DLS-LS-OCT. (A) Localized transverse speed $v_y(y, z)$ determined by DSubAp DOCT at the flow rate of 2.4 μL/min. The white arrow indicates the bottom glass-air interface where no flow exists. (B) Localized transverse speed $v_y(y, z)$ determined by DLS-LS-OCT at the same flow rate as (A). The red arrows show two discontinuous lines. (C) Comparison of the results of the two methods as a function of depth at different flow rates. The solid lines are the mean speeds determined by DSubAp DOCT and the opacity areas represent the 3-sigma uncertainties. The dot plots are the averaged speed determined by DLS-LS-OCT. The black arrow indicates the position of the bottom intralipid-glass interface where the transverse flow speed should be zero. (D) Speed comparison measured by DLS-LS-OCT and DSubAp DOCT at different depths.

arrows in Fig. 6(B) indicate two discontinuities that originate from defects in the top glass surface directly above the two discontinuous locations. The DSubAp DOCT is not affected since the two selected sub-apertures are away from the center. Figure 6(C) shows depth resolved transverse speeds $v_y(z)$ at different flow rates. The solid line and the opaque areas indicate the mean speeds determined by DSubAp DOCT and their 3-sigma uncertainty respectively. The dotted plots show the mean speeds measured with DLS-LS-OCT. The results obtained with the two methods are correlated very well in the depth range $z \in (5,\ 160)$ μm. The DLS-LS-OCT method cannot detect translational velocity under 0.3 mm/s precisely because mechanical motion and vibrations of the stage on which the flow phantom is mounted on induces additional decorrelation of the measured signal. Therefore, the lower flow speed detection limit of the DLS-LS-OCT method can be claimed as 0.3 mm/s. In the depth range $z \in (160,\ 200)\mu$m, the velocities estimated by DLS-LS-OCT are lower than those of DSubAp OCT except for the result at the flow rate of 0.6 μL/min, as indicated by the blue arrow. Since the DSubAp DOCT method is more sensitive to multiply scattered light, flow velocities measured with it are higher than the actual flow speed. This result suggests that DLS-LS-OCT might provide more precise measurement of flow velocity at greater depths inside scattering media. Due to low SNR, it was not possible to measure transverse flow velocity precisely with the DLS-LS-OCT method at depths $z > 200$ μm. Figure 6(D) shows the speed comparison measured by DLS-LS-OCT and DSubAp DOCT at different depths. All the dots are located at the $Y = X$ line within the error bar except for the speeds under 0.3 mm/s. This is consistent with what has been observed in Fig. 6(C).

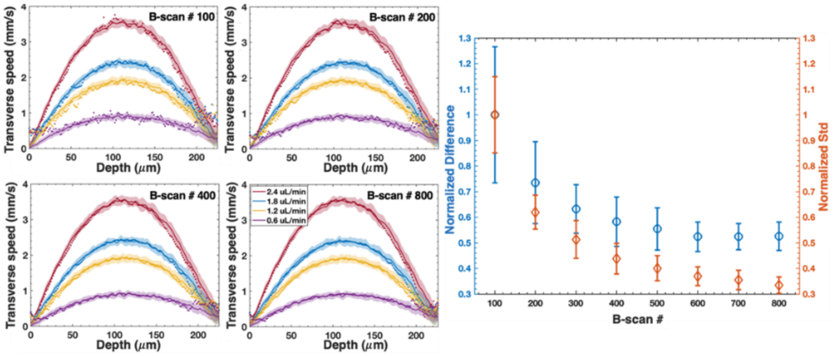

Fig. 7. Influence of B-scan number on the precision and robustness of DLS-LS-OCT. (Left) DLS-LS-OCT results estimated using different numbers of B-scans. The DSubAp DOCT results are shown by the solid lines as a reference. (Right) Normalized precision (blue) and robustness (orange) as a function of B-scan number.

We then investigate the influence of repeated B-scans numbers on the performance of DLS-LS-OCT. Too few B-scans cannot extract the true autocorrelation function, while too many are not necessary since the accuracy cannot be improved at a certain level due to the noise induced by inevitable mechanical motions. Figure 7 (Left) shows the DLS-LS-OCT results at different flow rates using the autocorrelation calculated with 100, 200, 400, and 800 repeated B-scans, respectively. The results calculated using 100 B-scans are imprecise. The performance improves with increasing the B-scan number, although the improvement from 400 to 800 is not significant. To provide a quantitative analysis of the relationship of the precision and robustness with the B-scan number, we define the precision and robustness of the DLS-LS-OCT as:

$$\begin{aligned} P &= \sum_i \left|\bar{v}_y(z_i) - v_{y,r}(z_i)\right| \\ R &= \sum_i \frac{1}{12-1} \sum_l^{12} \left(v_y(l,z_i) - \bar{v}_y(z_i)\right)^2 \end{aligned} \tag{21}$$

where $\overline{\mathrm{v_y}}(z_i) = \left\langle v_y(l, z_i)\right\rangle_l$ is the average of the DLS-LS-OCT's results of the 12 sub-tomograms, $v_{y,r}(z_i)$ is the mean speed of the DSubAp DOCT, and $z \in (0,\ 110)$ μm. The precision and robustness at the 4 different flow rates are calculated and the normalized precision and robustness as a function of B-scan number is shown in Fig. 7 (Right). Data shows that both the precision and the robustness improve significantly in the range of 100 to 600 B-scans, and the performance improvement is limited beyond 600. Therefore, 600 repeated B-scans were utilized in the subsequent studies.

4.2. Investigation of DLS-LS-OCT performance with axial velocity gradient and defocus

Flow with axial velocity gradient ∇v_z will result in accumulation of additional phase change in DSubAp DOCT [37] and additional decorrelation terms in DLS-OCT [25,40]. The transverse speeds estimated by both methods are imprecise unless special care is taken to account for these artifacts. The influence of axial velocity gradient on the performance of DLS-LS-OCT is investigated by comparing its results with those obtained with phase-based methods. As shown in Fig. 8(A), in our experiment, axial velocity gradient was introduced by tilting the glass capillary about the x-axis such that the Doppler angle is set as 87.9°, 85.3°, and 83.1°. The axial position of the glass capillary was set ~ 50 μm away from the location where the top glass-intralipid interface's signal in the center of y-direction reached the highest. Figure 8(B)-(D) shows the localized transverse speed $v_y(y, z)$ maps determined by DOCT, DSubAp DOCT, and DLS-LS-OCT at the flow rate of 1.8 μL/min with a Doppler angle of 85.3°, respectively. The DOCT's performance is the best among the three methods except for the fake velocity signal at the bottom glass-air interface. Figure 8(E)-(G) shows the transverse speeds $v_y(z)$ at different flow rates with a Doppler angle of 87.9°, 85.3°, and 83.1° respectively. The red and blue lines indicate the speeds determined by DOCT and DSubAp DOCT respectively and the opacity areas represent their 3-sigma uncertainties. The black dashed lines represent the results of DLS-LS-OCT. The DOCT is utilized as "gold standard" since the other two methods are sensitive to the velocity gradient induced distortion. The discontinuity of the DOCT and DSubAp DOCT's result at the flow rate of 2.4 μL/min in Fig. 8(G) is due to phase wrapping. The results from DLS-LS-OCT and DSubAp DOCT correlate very well with the "gold standard" at the Doppler angle of 87.9°. However, their performance worsens with increase of the Doppler angle, especially for the DLS-LS-OCT method at low SNR regions. The speed estimated by DSubAp DOCT is higher than that of DOCT from depth 0 to 100 μm and lower from depth 100 to 220 μm and the difference increase with the flow rate and decrease of the Doppler angle, which agrees with the theoretical prediction [37]. It is surprising that the results from DLS-LS-OCT and DSubAp DOCT are still highly overlapped in the depth range of 0 to 100 μm for all flow rates and Doppler angles, considering the reasons for the two methods' distortions are different. The fidelities of the DLS-LS-OCT at the three different Doppler angles are 0.964±0.014, 0.933±0.011, and 0.864±0.076, respectively. Figure 8(H)-(J) show the speed comparison measured by DLS-LS-OCT and DOCT at different depths, corresponding to Fig. 8(E)-(I) respectively. The speed is overestimated by DLS-LS-OCT at the Doppler angle of 85.3° and 83.1°, while the mismatch is negligible with the Doppler angle 87.9° except for the speed under 0.3 mm/s. The mismatch is dependent on the magnitude of the velocity gradient instead of the speed itself, as shown by the black arrow in Fig. 8(J). The speed estimated by DLS-LS-OCT is twice as large as the gold standard around 0.55 mm/s at the flow rate of 2.4 μL/min; however, the gap reduces with a decrease in flow rate as the location of same speed is closer to the capillary's central depth at which the velocity gradient is smaller.

Although there are many arguments suggesting that the decorrelation rate of DLS-OCT is only related to the beam waists and insensitive to the local beam sizes, it has been proven that the local beam sizes play an important role if axial velocity gradients exist [40]. We investigated the performance of the DLS-LS-OCT using the same Doppler angle for three different axial locations such that the local beam sizes are different. Figure 9(A) shows the transverse speeds $v_y(z)$ at different flow rates with a Doppler angle of 86.1°. The axial position of the glass capillary was set ~ 50 μm away from the location where the top glass-intralipid interface's signal in the center of y-direction reached the highest. In Fig. 9(B) and (C), the glass capillary's orientation was maintained the same, however, is position was translated upward axially 100 and 200 μm respectively such that the local beams sizes are significantly different from those in Fig. 9 (A), considering the Rayleigh range in the y-z plane is 48 μm. Figure 9(D)-(F) show the speed comparison measured by DLS-LS-OCT and DOCT at different depths, corresponding to Fig. 9(A)-(C) respectively. The mismatch between the DLS-LS-OCT's results and the "gold standard" from depth 0 to 100 μm increases with increase of the local beam size. The fidelities of the DLS-LS-OCT results at the three different axial positions are 0.927±0.004, 0.901±0.011, and 0.884±0.010 respectively. The results in Figs. 8 and 9 qualitatively show that the accuracy of DLS-LS-OCT is influenced by the axial velocity gradients as well as the local beam sizes. Nevertheless, this result correlates very well with the DSubAp DOCT at the high SNR regions. This result is quite interesting because theoretically the distortions in the two methods are different. In DSubAp DOCT, the phase error, $\beta\nabla_y v_z$, comes from the lateral shifts induced by of the two sub-apertures [37], where β is the axial distance from the focal plane and ∇_y denotes the spatial gradient along the y-direction. In the DLS-LS-OCT results, the additional decay arises from the integration of non-uniform motion over the volume confined by the local optical beam size

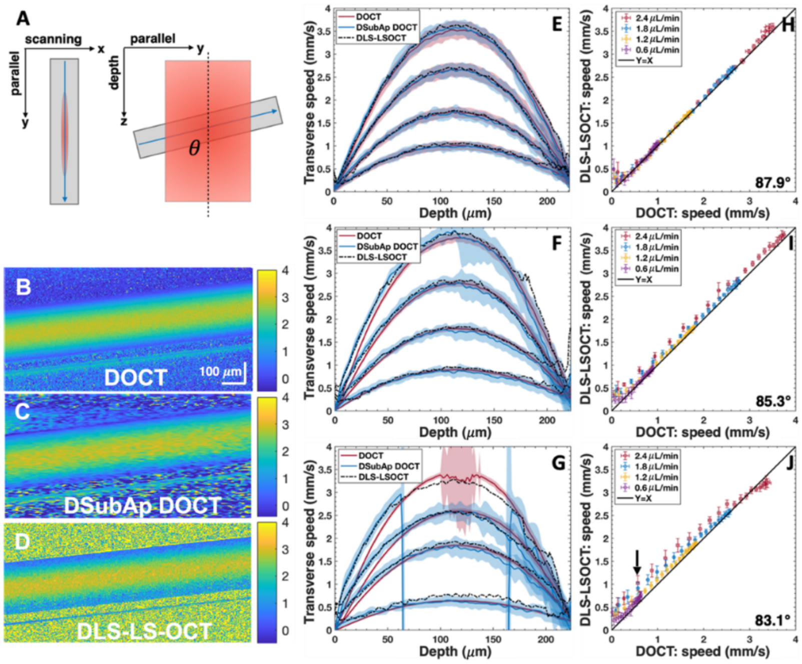

Fig. 8. Comparison of the results of DOCT, DSubAp DOCT, and DLS-LS-OCT at different Doppler angles. (A) Schematic of the illumination plane with respect to the flow direction. (B-D) Typical localized transverse speed $v_y(y, z)$ maps determined by DOCT, DSubAp DOCT, and DLS-LS-OCT at the flow rate of 1.8 μL/min with a Doppler angle of 85.3°. (E)-(G) Depth resolved transverse speed $v_y(z)$ at different flow rates with a Doppler angle of 87.9°, 85.3°, and 83.1°, respectively. The red and blue solid lines indicate the speeds determined by DOCT and DSubAp DOCT respectively and the opacity areas represent their 3-sigma uncertainties. The results of DLS-LS-OCT are shown by the black dash line. (H)-(J) The speed comparison measured by DLS-LS-OCT and DOCT at different depths, corresponding to (E)-(I) respectively.

and its coherence gate [40]. The index of the additional decorrelation term is proportional to $(\omega_y^2 - {\omega_y{'}}^2)(\nabla_y v_z)^2$ [40], and other gradient induced terms should be canceled in $G_1(t)$. ω_y and $\omega_y{'}$ are the local beam sizes of the original and low-resolution OCT signals respectively. One reason why the two results coincide might be that they have been averaged over 12 sub-tomograms and each sub-tomogram's defocus are slightly different since the glass capillary is tilted.

In principle, both methods' distortions can be compensated by digitally correcting the defocus aberration across the B-scans. Without defocus, the lateral shifts are eliminated in DSubAp DOCT. For the DLS-LS-OCT, since $\omega_y = \sigma_y$ and $\omega_y{'} = \sigma_y{'}$ are constant after defocus aberration correction, the additional decay term can be removed by introducing another low-resolution OCT tomogram whose resolution meets the condition $\sigma_y{''} + \sigma_y = 2\sigma_y{'}$. However, since the phantom's flow lacks structural contrasts, compensating the aberration using digital adaptive optics is almost impossible. Furthermore, eliminating the additional decorrelation term requires a more precise autocorrelation function, which necessitates higher SNR and averaging over larger number of B-scans. Therefore, compensating the velocity gradient induced error is still changeling in OCT based flow velocimetry.

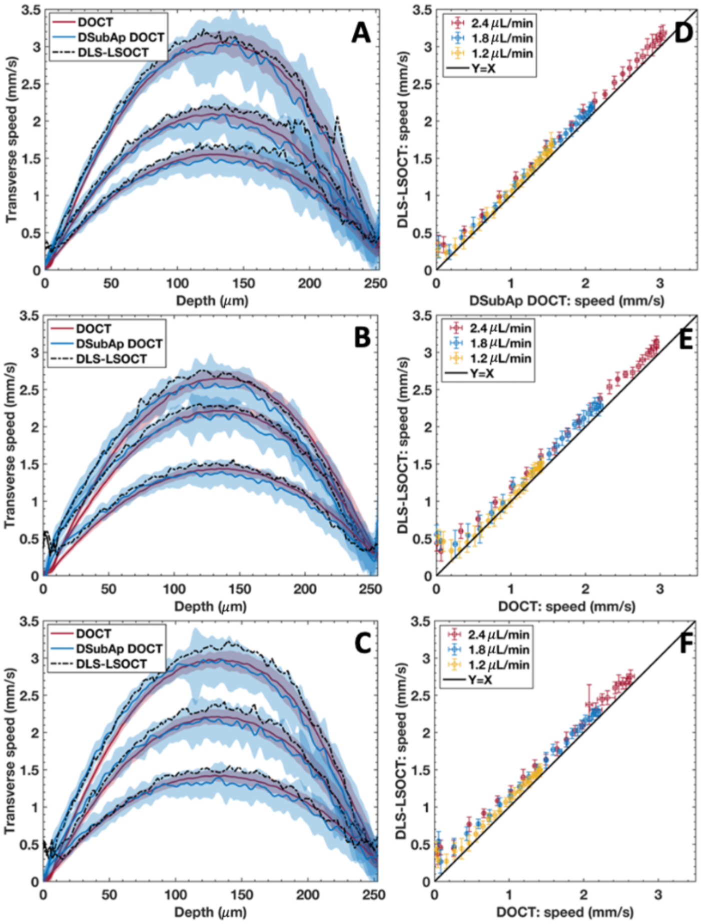

Fig. 9. Comparison of the velocity results calculated with the DOCT, DSubAp DOCT, and DLS-LS-OCT approaches at different depths in the intralipid. (A) Depth resolved transverse speed $v_y(z)$ at different flow rates with a Doppler angle of 86.1°. The red and blue solid lines indicate the speeds determined by DOCT and DSubAp DOCT respectively and the opacity areas represent their 3-sigma uncertainties. The results of DLS-LS-OCT are shown by the black dash line. (B) and (C) Depth resolved transverse speed $v_y(z)$ measured with the same Doppler angle at two different out of focus depths. (D)-(F) The speed comparison measured by DLS-LS-OCT and DOCT at different depths, corresponding to (A)-(C) respectively.

4.3. Detection of the spatially resolved velocity in the beam illuminating plane

Figure 10(A) shows a customized PDMS microfluidic phantom. The black box indicates a T-shape bifurcated structure at which the 2D transverse velocity distribution is measured. Figure 10(B) shows the magnified ROI in Fig. 10(A). The dashed and solid lines in red and orange denote the four locations where B-scans were recorded with LS SD-OCT. The blue arrows indicate the direction of the flow. Figure 10(C) shows the log-scaled B-scan amplitude images of the 4 selected locations. The imaging beam was incident normally to the phantom's surface and the intralipid flow rate was set to 7.5 μL/min. The discontinuity of the intralipid-glass interface in (C3) and (C4) is the result of a mismatch of the refraction index of the intralipid solution and PDMS material. Figure 10(D) shows the localized transverse velocity $v_y(y, z)$ determined by DLS-LS-OCT. A binary mask is applied to block out the noise-only regions. The phase difference determined with DSubAp DOCT using two half sub-apertures are utilized to determine the direction of v_y. Due to the lower speed detection limit, the transverse speed lower than 0.3 mm/s is overestimated in DLS-LS-OCT, which leads to an artificial discontinuity indicated by the black arrow in Fig. 10(D1). Figure 10(E) shows the localized transverse velocity $v_y(y, z)$ determined by DSubAp DOCT.

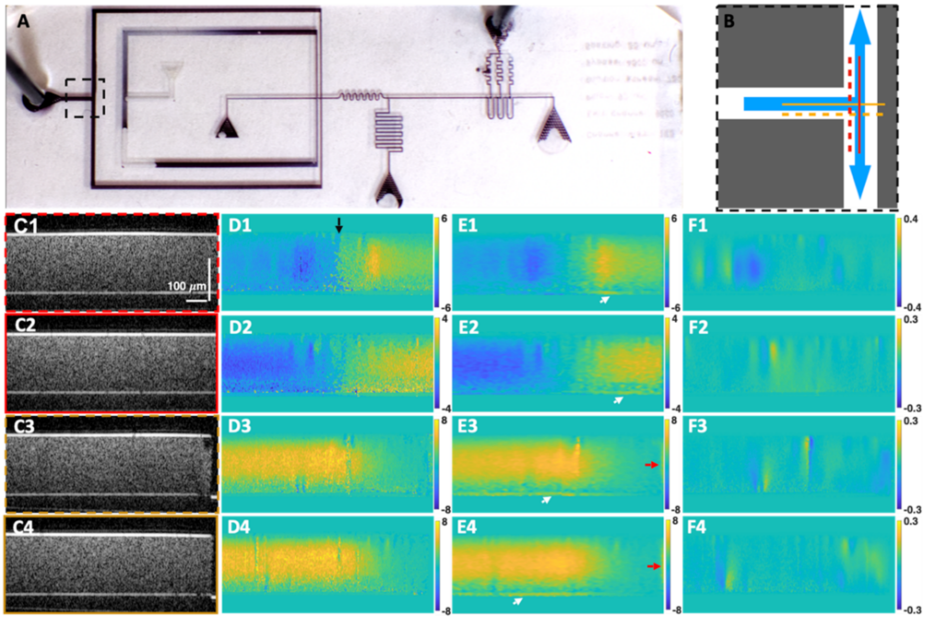

Fig. 10. Localized transverse velocity detection of a T-shape bifurcated structure. The flow rate is 7.5 μL/min. (A) Image of the custom microfluid phantom. The phantom is filled with black ink for better visualization of the structure. The black box shows the selected ROI. (B) Magnification of the ROI in (A). The solid and dashed lines indicate the B-scans. The blue arrows show the flow directions. (C) Typical log-scale B-scan images of the 4 locations labelled in (B). (D, E) Transverse flow speed $v_y(y, z)$ determined by DLS-LS-OCT and DSubAp DOCT respectively. (F) Axial velocity $v_z(y, z)$ due to phantom surface defects or attached air bubbles.

Besides the low resolution, results from the DSubAp DOCT methods also show two artefact signals indicated by the white and red arrow respectively. The artificial signals marked by the white arrows arise from the additional phase associated with detection of multiply scattered light in the intralipid [41]. Since this artifact depends both on the presence of multiply scattered light and the speed of the scatters above the location of the signal, it is more pronounced for greater depths and faster flows. The artefacts at the same location in Fig. 10(D) are much smaller than those in Fig. 10(E). Thus, DLS-LS-OCT seems more robust than DSubAp DOCT in terms of multi-scattering. The other artefact signals marked by the red arrow originate from the defocus-indued lateral shifts since the sub-apertures are away from the center. Figure 10(F) shows the localized axial velocity $v_z(y, z)$ which might come from the phantom surface defects or attached air bubbles. The proposed DLS-LS-OCT has successfully detected the localized transverse velocity distribution $v_y(y, z)$ of the T-shape bifurcated structure at different locations. Compared to the results obtained with the DSubAp-DOCT, DLS-LS-OCT shows finer vortex structures and weaker artefact signals corresponding to multiply scattered light.

4.4. Estimating the transverse flow direction

Although it was shown in section 4.1 that the diffusion compensation method is unsuitable for precise measurement of the transverse flow speed with the current LS SD-OCT system, it can still be used to determine the direction of the transverse flow at the ensemble level. Consider the situation where the flow velocity is confined in the xy-plane and the angle between the flow and beam illumination is θ, as shown in Fig. 11(A). The diffusion compensated autocorrelation and the ratio between the autocorrelation functions of the original and low-resolution OCT signals can be expressed as:

$$\begin{aligned}\tilde{g}_1(\mathrm{n}\tau) &= \gamma\exp[-(\frac{v_x^2}{\sigma_x^2}+\frac{v_y^2}{\sigma_y^2})\mathrm{n}^2\tau^2]\\ &= \gamma\exp(-\Gamma\mathrm{n}^2)\\ G_1(\mathrm{n}\tau) &= \exp[-(1/\sigma_y^2-1/\sigma_y'^2)v_y^2\mathrm{n}^2\tau^2]\\ &= \exp(-\Gamma_y\mathrm{n}^2)\end{aligned} \tag{22}$$

where $\Gamma = -\left(\frac{v_x^2}{\sigma_x^2}+\frac{v_y^2}{\sigma_y^2}\right)\tau^2$ and $\Gamma_y = -(1/\sigma_y^2 - 1/\sigma_y{'}^2)v_y^2\tau^2$ are the dimensionless decorrelation strengths which depend on the localized speeds, resolutions, and time resolution of the system. Together with $\vec{v} = v_0\cos\theta\hat{x} + v_0\sin\theta\hat{y}$ the ratio of Γ and Γ_y can be simplified as:

$$\frac{\Gamma}{\Gamma_y} = \frac{1/\sigma_x^2}{1/\sigma_y^2 - 1/\sigma\prime_y^2}\tan^2\theta + \frac{1/\sigma_y^2}{1/\sigma_y^2 - 1/\sigma\prime_y^2} \tag{23}$$

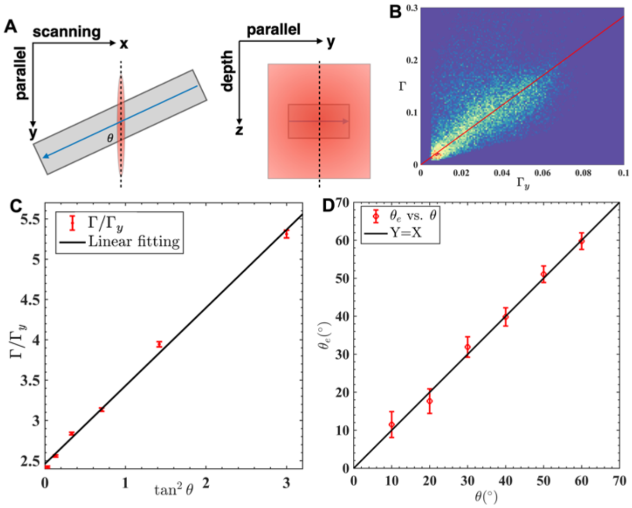

Fig. 11. (A) Schematic of the illumination plane with respect to the flow direction. (B) Representative pixel-to-pixel scatter plot of common pixels of the decorrelation strength maps $\Gamma(y,z)$ and $\Gamma_y(y,z)$ with value $|\Gamma|>|\Gamma_y|>0.005$. The solid red line shows the linear fitting of the selected data. (C) Fitted ratio Γ/Γ_y as a function of $\tan^2\theta$. (D) Estimated transverse flow direction vs. the preset angle.

If the resolution parameters are constants, Γ/Γ_y should be independent with its location. Figure 11(B) shows a representative pixel-to-pixel scatter plot of the decorrelation strength maps $\Gamma(y,z)$ and $\Gamma_y(y,z)$ with $\theta = 30°$. We determine the ratio Γ/Γ_y by linear fitting the scatter plot ($|\Gamma|>|\Gamma_y|>0.005$). The flow is measured for preset angles ranging from 10° to 60° and flow rate of

8 μL/min. The ratio Γ/Γ_y vs. $\tan^2\theta$ is shown in Fig. 11(C). Since the resolution in the x-direction is unavailable, we estimated the two coefficients, $\frac{1/\sigma_x^2}{1/\sigma_y^2-1/\sigma_y'^2}$ and $\frac{1/\sigma_y^2}{1/\sigma_y^2-1/\sigma_y'^2}$, by linear fitting and then substitute back to estimate the flow direction, as shown in Fig. 11(D).

5. Discussion

In this study, we demonstrated a novel decorrelation-based method for measurement of localized transverse flow using a LS SD-OCT system, compared the precision of the method with that of other methods such as DOCT and DSubAp-DOCT, and investigated different factors that can affect the precision of the new method for measuring transverse flow speed. The effective A-scan acquisition rate of our current LS SD-OCT system is 1.5 MHz, which is about 30 times faster than the OCT systems used for DLS-OCT reported previously [9,33,40]. This method provides an accurate transverse flow velocity measurement independent of the diffusional motion, translational motions perpendicular to the y-direction, and the noise-induced distortion relating to the local SNR.

We calculated the quasi-localized resolution parameters $\sigma_y(l,z)$ and $\sigma_y'(l,\ z)$ based on the spatial autocorrelation for each dataset separately following the method described in [32]. Since calculating the spatial autocorrelation requires a set of data from different lateral positions, the resolution parameters cannot be spatially resolved along the y-direction. Instead, they are assumed to be constants along the y-direction within each sub-tomogram. Compared with other fitting methods using DLS-OCT, DLS-LS-OCT shows extraordinary precision in determining the transverse flow speed where no axial velocity gradient exists. To our best knowledge, this is the first time that the DLS-OCT shows precise velocity distributions based on the temporal autocorrelation of B-scans instead of flow dynamic parameters composed of diffusional and translational motions [20,29]. Although some fast point-scan SD-OCT [42,43] can reach B-scan rates similar to that of LS SD-OCT by significantly reducing the A-scan number within each B-scan, the additional decorrelation due to the scan jitter results in fewer data points above the noise level and must be accounted for [32]. In the case where axial velocity gradient exists, results generated by both DLS-LS-OCT and DSubAp DOCT methods are distorted compared to those acquired with DOCT. Our results support the theoretical prediction that the local beam sizes, along with presence of an axial velocity gradient, will affect the precision of the estimated flow velocity [40].

We also showed that DLS-LS-OCT has several advantages over DSubAp DOCT. DLS-LS-OCT shows finer transverse velocity distribution with better lateral resolution. The DSubAp DOCT's lateral resolution is mainly limited by its sub-apertures' size. Since finding the effective angle separation of two large sub-apertures is difficult, we limited the size of two sub-apertures to 1/10 of the full aperture. Furthermore, DLS-LS-OCT uses complex OCT signal which is less sensitive to multi-scattering as compared to Doppler OCT. Although the influence of multiple scattering on the precision of DLS-OCT flow velocity measurement has not been theoretically derived, our experimental results show that the artificial velocity signals that appear in the DLS-LS-OCT data are weak compared to artefacts detected with DSubAp-DOCT at the intralipid-glass interfaces. In addition, the DSubAp DOCT's upper transverse speed detection limit is highly sensitive to the axial velocity since the wavevector's axial component is dominated. Axial motion can lead to phase wrapping even at low speed (~ 0.44 mm/s in this study), resulting in ambiguity in the lateral velocity calculation. In contrast, DLS-LS-OCT's transverse velocity detection range is not affected significantly by a small axial velocity component as long as the axial and lateral resolutions are comparable.

There are still several limitations to our study. For example, the time required for estimation of the precise temporal autocorrelation is significantly longer than the time needed for phase extraction in phase-based methods. Our analysis shows that 600 repeated B-scans (T = 0.2

second) are necessary to achieve a credible speed estimation, as the method requires ergodicity. This can be alleviated by spatial averaging. The speed detection range is limited in this study, and is in the range of ~0.3-4 mm/s. A higher time resolution can help to increase the upper limit, and it can be achieved by reducing the FOV or employing a faster area camera. Modifying resolution parameters is another choice if high spatial resolution is not necessary. Furthermore, the effect of axial velocity gradient along the line-illumination direction is not compensated here. The axial velocity gradient can introduce an additional decorrelation term, leading to a significant distortion in the estimated speed. Another limitation of the proposed method is that the flow velocity cannot be determined precisely in the x-direction because the quadratic term fitting is problematic with insufficient SNR and time resolution. Further increase in the optical power of the imaging beam and improvement of the system's time resolution can enhance the performance of DLS-OCT DC, which in turn can improve the accuracy of measuring v_x.

6. Conclusion

We proposed a novel decorrelation-based approach to measuring localized transverse flow measurement using LS SD-OCT and investigated various factors that affect its precision. By altering the lateral resolution digitally and fitting them into our DLS-LS-OCT theoretical model, we were able to detect accurately transverse flow velocity independently from the diffusion motion of the flow scatterers, translational motion perpendicular to the y-direction, and noise-induced distortion related to the local SNR. The proposed method extends the current DLS-OCT techniques in terms of distinguishing the transverse velocity components. It can be potentially extended to measure the three-dimensional flow velocity and be applied to *ex-vivo* and *in-vivo* applications.

Funding. Canada First Research Excellence Fund; Canadian Institutes of Health Research (446387); Natural Sciences and Engineering Research Council of Canada (312037); National Research Foundation Singapore (NRF2019-THE002-0006); National Medical Research Council (CG/C010A/2017_SERI, MOH-001015-00).

Acknowledgments. The microfluidic phantom used in this study was provided by the research groups of Prof. Carolyn L. Ren at the University of Waterloo.

Disclosures. The authors declare no conflicts of interest related to this article.

Data availability. Data underlying the results presented in this paper are not publicly available at this time but may be obtained from the authors upon reasonable request.

Supplemental document. See Supplement 1 for supporting content.

References

1. W. Drexler and J. G. Fujimoto, eds., *Optical Coherence Tomography*, 2nd ed. (Springer Cham, 2015).
2. R. K. Wang, S. L. Jacques, Z. Ma, S. Hurst, S. R. Hanson, and A. Gruber, "Three dimensional optical angiography," Opt. Express **15**(7), 4083 (2007).
3. A. H. Kashani, C.-L. Chen, J. K. Gahm, F. Zheng, G. M. Richter, P. J. Rosenfeld, Y. Shi, and R. K. Wang, "Optical coherence tomography angiography: a comprehensive review of current methods and clinical applications," Prog. Retinal Eye Res. **60**, 66–100 (2017).
4. B. Tan, R. Sim, J. Chua, D. W. K. Wong, X. Yao, G. Garhöfer, D. Schmidl, R. M. Werkmeister, and L. Schmetterer, "Approaches to quantify optical coherence tomography angiography metrics," Ann Transl Medicine **8**(18), 1205 (2020).
5. B. Tan, J. Chua, E. Lin, J. Cheng, A. Gan, X. Yao, D. W. K. Wong, C. Sabanayagam, D. Wong, C. M. Chan, T. Y. Wong, L. Schmetterer, and G. S. Tan, "Quantitative microvascular analysis with wide-field optical coherence tomography angiography in eyes with diabetic retinopathy," JAMA Netw. Open **3**(1), e1919469 (2020).
6. Z. Chen, T. E. Milner, S. Srinivas, X. Wang, A. Malekafzali, M. J. C. van Gemert, and J. S. Nelson, "Noninvasive imaging of in vivo blood flow velocity using optical Doppler tomography," Opt. Lett. **22**(14), 1119 (1997).
7. S. Yazdanfar, A. M. Rollins, and J. A. Izatt, "Imaging and velocimetry of the human retinal circulation with color Doppler optical coherence tomography," Opt. Lett. **25**(19), 1448 (2000).
8. R. Leitgeb, L. F. Schmetterer, M. Wojtkowski, C. K. Hitzenberger, M. Sticker, and A. F. Fercher, "Flow velocity measurements by frequency domain short coherence interferometry," *P Soc Photo-opt Ins* 16–21 (2002).
9. J. Lee, W. Wu, J. Y. Jiang, B. Zhu, and D. A. Boas, "Dynamic light scattering optical coherence tomography," Opt. Express **20**(20), 22262–22277 (2012).

10. C. Joo and J. F. de Boer, "Field-based dynamic light scattering microscopy: theory and numerical analysis," Appl. Opt. **52**(31), 7618 (2013).
11. B. Braaf, M. G. O. Gräfe, N. Uribe-Patarroyo, B. E. Bouma, B. J. Vakoc, J. F. de Boer, S. Donner, and J. Weichsel, "OCT-based velocimetry for blood flow quantification," in *High Resolution Imaging in Microscopy and Ophthalmology, New Frontiers in Biomedical Optics* (2019), pp. 161–179.
12. R. A. Leitgeb, R. M. Werkmeister, C. Blatter, and L. Schmetterer, "Doppler optical coherence tomography," Prog. Retinal Eye Res. **41**, 26–43 (2014).
13. R. M. Werkmeister, N. Dragostinoff, M. Pircher, E. Götzinger, C. K. Hitzenberger, R. A. Leitgeb, and L. Schmetterer, "Bidirectional Doppler Fourier-domain optical coherence tomography for measurement of absolute flow velocities in human retinal vessels," Opt. Lett. **33**(24), 2967 (2008).
14. R. Haindl, W. Trasischker, B. Baumann, M. Pircher, and C. K. Hitzenberger, "Three-beam Doppler optical coherence tomography using a facet prism telescope and MEMS mirror for improved transversal resolution," J. Mod. Opt. **62**(21), 1781–1788 (2015).
15. C. J. Pedersen, D. Huang, M. A. Shure, and A. M. Rollins, "Measurement of absolute flow velocity vector using dual-angle, delay-encoded Doppler optical coherence tomography," Opt. Lett. **32**(5), 506 (2007).
16. H. Spahr, C. Pfäffle, P. Koch, H. Sudkamp, G. Hüttmann, and D. Hillmann, "Interferometric detection of 3D motion using computational subapertures in optical coherence tomography," Opt. Express **26**(15), 18803–18816 (2018).
17. L. Ginner, A. Wartak, M. Salas, M. Augustin, M. Niederleithner, L. M. Wurster, and R. A. Leitgeb, "Synthetic subaperture-based angle-independent Doppler flow measurements using single-beam line field optical coherence tomography in vivo," Opt. Lett. **44**(4), 967 (2019).
18. B. J. Berne and R. Pecora, Dy*namic Light Scattering: With Applications to Chemistry*, *Biology, and Physics* (Dover Publications, 2000).
19. W. Zhou, O. Kholiqov, S. P. Chong, and V. J. Srinivasan, "Highly parallel, interferometric diffusing wave spectroscopy for monitoring cerebral blood flow dynamics," Optica **5**(5), 518 (2018).
20. V. J. Srinivasan, H. Radhakrishnan, E. H. Lo, E. T. Mandeville, J. Y. Jiang, S. Barry, and A. E. Cable, "OCT methods for capillary velocimetry," Biomed. Opt. Express **3**(3), 612–629 (2012).
21. J. Tang, D. D. Postnov, K. Kilic, S. E. Erdener, B. Lee, J. T. Giblin, T. L. Szabo, and D. A. Boas, "Functional ultrasound speckle decorrelation-based velocimetry of the brain," Adv. Sci. (Weinheim, Ger.) **7**(18), 2001044 (2020).
22. D. A. Boas, K. K. Bizheva, and A. M. Siegel, "Using dynamic low-coherence interferometry to image Brownian motion within highly scattering media," Opt. Lett. **23**(5), 319 (1998).
23. K. K. Bizheva, A. M. Siegel, and D. A. Boas, "Path-length-resolved dynamic light scattering in highly scattering random media: The transition to diffusing wave spectroscopy," Phys. Rev. E **58**(6), 7664–7667 (1998).
24. K. K. Bizheva, A. M. Siegel, A. K. Dunn, and D. A. Boas, "Detection of multiply scattered light in optical coherence microscopy," in *Waves and Imaging through Complex Media* (Springer, 2001), pp. 277–298.
25. N. Weiss, T. G. van Leeuwen, and J. Kalkman, "Localized measurement of longitudinal and transverse flow velocities in colloidal suspensions using optical coherence tomography," Phys. Rev. E **88**(4), 042312 (2013).
26. N. Uribe-Patarroyo, M. Villiger, and B. E. Bouma, "Quantitative technique for robust and noise-tolerant speed measurements based on speckle decorrelation in optical coherence tomography," Opt. Express **22**(20), 24411–24429 (2014).
27. M.-T. Tsai, T.-T. Chi, H.-L. Liu, F.-Y. Chang, C.-H. Yang, C.-K. Lee, and C.-C. Yang, "Microvascular imaging using swept-source optical coherence tomography with single-channel acquisition," Appl. Phys. Express **4**(9), 097001 (2011).
28. W. Choi, E. M. Moult, N. K. Waheed, M. Adhi, B. Lee, C. D. Lu, T. E. de Carlo, V. Jayaraman, P. J. Rosenfeld, J. S. Duker, and J. G. Fujimoto, "Ultrahigh-speed, swept-source optical coherence tomography angiography in nonexudative age-related macular degeneration with geographic atrophy," Ophthalmology **122**(12), 2532–2544 (2015).
29. S. B. Ploner, E. M. Moult, W. Choi, N. K. Waheed, B. Lee, E. A. Novais, E. D. Cole, B. Potsaid, L. Husvogt, J. Schottenhamml, A. Maier, P. J. Rosenfeld, J. S. Duker, J. Hornegger, and J. G. Fujimoto, "Toward quantitative optical coherence tomography angiography," Retina **36**(1), S118–S126 (2016).
30. T. W. Taylor and C. M. Sorensen, "Gaussian beam effects on the photon correlation spectrum from a flowing Brownian motion system," Appl. Opt. **25**(14), 2421 (1986).
31. S. Makita, F. Jaillon, I. Jahan, and Y. Yasuno, "Noise statistics of phase-resolved optical coherence tomography imaging: single-and dual-beam-scan Doppler optical coherence tomography," Opt. Express **22**(4), 4830 (2014).
32. K. Kurokawa, S. Makita, Y.-J. Hong, and Y. Yasuno, "Two-dimensional micro-displacement measurement for laser coagulation using optical coherence tomography," Biomed. Opt. Express **6**(1), 170–190 (2015).
33. N. Weiss, T. G. van Leeuwen, and J. Kalkman, "Simultaneous and localized measurement of diffusion and flow using optical coherence tomography," Opt. Express **23**(3), 3448–3459 (2015).
34. L. Han, B. Tan, Z. Hosseinaee, L. K. Chen, D. Hileeto, and K. Bizheva, "Line-scanning SD-OCT for in-vivo, non-contact, volumetric, cellular resolution imaging of the human cornea and limbus," Biomed. Opt. Express **13**(7), 4007 (2022).
35. M. Courtney, X. Chen, S. Chan, T. Mohamed, P. P. N. Rao, and C. L. Ren, "Droplet microfluidic system with on-demand trapping and releasing of droplet for drug screening applications," Anal. Chem. **89**(1), 910–915 (2017).

36. L. Ginner, A. Kumar, D. Fechtig, L. M. Wurster, M. Salas, M. Pircher, and R. A. Leitgeb, "Noniterative digital aberration correction for cellular resolution retinal optical coherence tomography in vivo," Optica **4**(8), 924–931 (2017).
37. H. Spahr, C. Pfäffle, G. Hüttmann, and D. Hillmann, "Artifacts in speckle tracking and multi-aperture Doppler OCT imaging of lateral motion," Opt. Lett. **44**(6), 1315 (2019).
38. J. Kalkman, R. Sprik, and T. G. van Leeuwen, "Path-length-resolved diffusive particle dynamics in spectral-domain optical coherence tomography," Phys. Rev. Lett. **105**(19), 198302 (2010).
39. V. M. Kodach, D. J. Faber, J. van Marle, T. G. van Leeuwen, and J. Kalkman, "Determination of the scattering anisotropy with optical coherence tomography," Opt. Express **19**(7), 6131 (2011).
40. N. Uribe-Patarroyo and B. E. Bouma, "Velocity gradients in spatially resolved laser Doppler flowmetry and dynamic light scattering with confocal and coherence gating," Phys. Rev. E **94**(2), 022604 (2016).
41. J. Kalkman, A. V. Bykov, D. J. Faber, and T. G. van Leeuwen, "Multiple and dependent scattering effects in Doppler optical coherence tomography," Opt. Express **18**(4), 3883 (2010).
42. B. Tan, Z. Hosseinaee, L. Han, O. Kralj, L. Sorbara, and K. Bizheva, "250 kHz, 1.5 µm resolution SD-OCT for in-vivo cellular imaging of the human cornea," Biomed. Opt. Express **9**(12), 6569–6583 (2018).
43. M. Münter, H. Schulz-Hildebrandt, M. Pieper, P. König, and G. Hüttmann, "4D microscopic optical coherence tomography imaging of ex vivo mucus transport," Opt Coherence Imaging Techniques Imaging Scatt Media Iii **11078**, 36–1107811–5 (2019).